Optics and Lasers in Engineering 186 (2025) 108769

Contents lists available at ScienceDirect

Optics and Lasers in Engineering

journal homepage: www.elsevier.com/locate/optlaseng

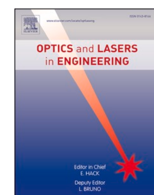

Robust vertical scanning interferometry at a long coherence length

Hang Zhao [a], Yijun Xie [b], Renlong Zhu [b], Zhengqiong Dong [b], Xuanze Wang [b], Shiyuan Liu [a], Jinlong Zhu [a,c,d,*]

[a] State Key Laboratory of Intelligent Manufacturing Equipment and Technology, Huazhong University of Science and Technology, Wuhan 430074, PR China
[b] School of Mechanical Engineering, Hubei University of Technology, Wuhan 430068, PR China
[c] Research Institute of Huazhong University of Science and Technology in Shenzhen, Shenzhen 518057, PR China
[d] Optics Valley Laboratory, Wuhan 430074, PR China

ARTICLE INFO

Keywords:
Vertical scanning interferometry
Surface recovery
Coherence envelope
Zero optical path difference

ABSTRACT

Vertical scanning interferometry (VSI) is a non-invasive and effective method for three-dimensional (3D) measurement and surface characterization. A fast and accurate surface recovery algorithm based on interference signal pre-filtering and statistical phase compensation is proposed for VSI working at the long coherence length. The simulated and experimental results demonstrated that the proposed algorithm is more robust than conventional methods such as white light phase shifting interferometry (WLPSI) and Hilbert transform in terms of intensity noise and positioning noise at the condition of a light source with a long coherence length. The measured standard deviation (SD) using the proposed algorithm for the standard step sample is 1.5 nm, while the SDs measured by conventional WLPSI and Hilbert transform are 171.4 nm and 30.7 nm respectively, which demonstrated the high accuracy of the proposed algorithm under the condition of a long coherence length.

1. Introduction

The rapid development and extensive applications of optical components and micro-electromechanical system (MEMS) devices demand advanced measurement techniques with extreme accuracy [1–3], in order to ensure their performance and reliability as well as to optimize the manufacturing process [4]. Optical metrology techniques, such as vertical scanning interferometry (VSI), phase shifting interferometry (PSI), focus variation microscopy and confocal microscopy, have been widely employed for surface profile measurement and dimension metrology [5,6]. PSI and VSI are the two primary optical interferometry methods that have high-resolution, widefield and nondestructive characteristics [7]. Single-wavelength PSI has the issue of unidentifiable zero-order fringe because of the periodic intensity response [8]. As a result, the single-wavelength PSI suffers from 2π ambiguity despite the measurement precision can reach up to $\lambda/1000$ [9], which limit its application in the measurement of only smooth surfaces. To overcome the phase ambiguity for measuring non-smooth structures, multiple-wavelength PSI has been proposed to extend the unambiguous range via equivalent wavelength [10,11], which in turn complicates the illumination system [12]. In contrast, VSI using a broadband light source with short coherence length has been more extensively applied in the measurement of discontinuous structures and rough surfaces. The interference signal of VSI only appears within the coherent length and presents the maximal modulation value when the optical path difference between the reference and object beams is zero [13]. The position of coherence envelope peak is regarded as position of zero optical path difference (ZOPD). Therefore, VSI scans the object vertically and analyses the peaks of coherence envelopes for each pixel, after which the surface height distribution can be reconstructed by positioning the vertical position of envelope peaks without phase ambiguity [13,14].

White LED has been widely utilized in VSI because it has greater power, longer lifetime, low heat dissipation and compactness [15], compared with tungsten-halogen lamps. However, the wide spectrum introduces some typical problems due to dispersion effects and lateral chromatic aberrations [16,17], such as measurement errors in the envelope evaluation and ghost steps in the phase evaluation, especially for tilted and curved surface [6,18,19]. Moreover, the bimodal feature of a white LED affects the envelope curve of interference signal, which brings a great challenge to envelope peak extraction [20,21]. Although shortening the bandwidth of a white LED using a bandpass filter may alleviate the aforementioned issues, the increased coherence length means that the fringe packet and the full width at half maximum (FWHM) of envelope curve are wider, which increases the difficulty of positioning the

* Corresponding author.
E-mail address: jinlongzhu03@hust.edu.cn (J. Zhu).

https://doi.org/10.1016/j.optlaseng.2024.108769
Received 28 May 2024; Received in revised form 14 October 2024; Accepted 9 December 2024
Available online 16 December 2024
0143-8166/© 2024 Elsevier Ltd. All rights reserved, including those for text and data mining, AI training, and similar technologies.

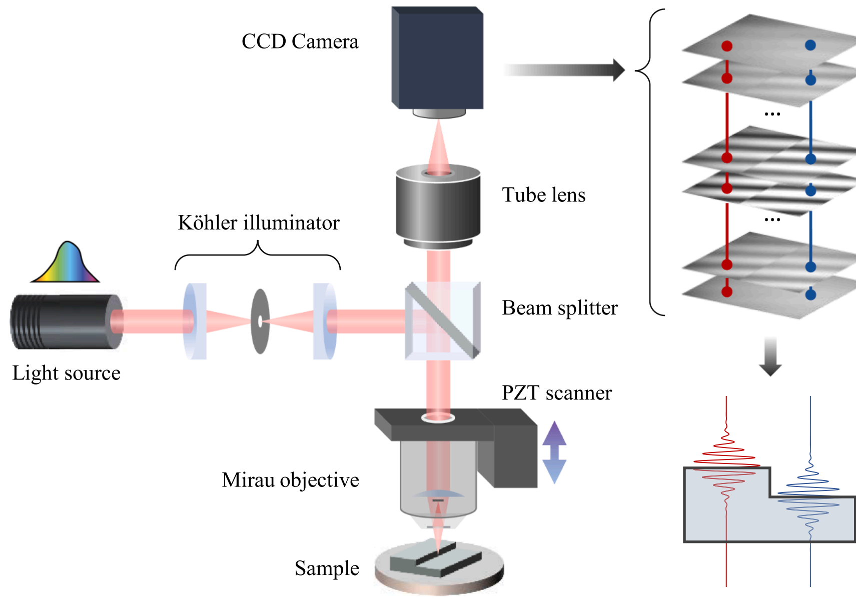

Fig. 1. Schematic diagram of a representative VSI system.

envelope peak and ZOPD, especially when multiple error sources exist in the system, such as light source fluctuation, the uncertainty of piezoelectric transducers (PZT), floor vibrations and air turbulence. According to the theory of envelope-peak-sensing, the surface recovery algorithms of VSI can be divided into direct and indirect methods. Typical direct methods involve interpolation method, centroid method [22] and spatial frequency domain analysis method [23], while the representative indirect methods include polynomial fitting method [24], Fourier transform method [25], Hilbert transform method [26] and wavelet transform method [12]. Although the envelope peak position is strongly related to the position of ZOPD, the position of the envelope peak is not exactly the same as the ZOPD's. Since the white light interferogram includes both fringe and coherence envelope features, the improved approach called white light PSI (WLPSI) combines VSI and PSI to obtain the position of ZOPD nearest to the envelope peak. Shen et al. [13] proposed nine- or eleven-steps phase-shifting algorithms based on local linear conditions of envelope function to determine the position of ZOPD. Vo et al. [1] combined white light phase shifting and fast Fourier transform envelope-peak-sensing to solve the problem of positioning error in the maximum modulation and batwing effect at the step edges. Chen et al. [8] introduced a white light phase-shifting measurement method based on the optimal sampling point and the centroid of modulation for accurate surface reconstruction under the scanning error of PZT. However, the aforementioned algorithms, developed for interference signals with short fringe packet, suffer from the degeneration of accuracy and robustness at the condition of a long coherent length.

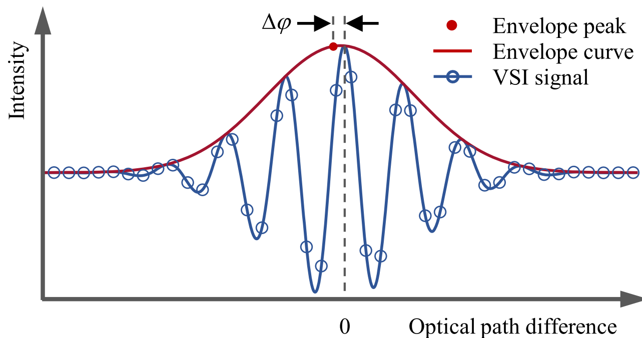

Fig. 2. Illustration of the bias between the envelope peak and the ZOPD position.

In this paper, we use a green LED instead of a white LED to alleviate the dispersion effects as well as the impact of bimodal spectral distribution on envelope peak extraction. To tackle the challenge of envelope peak extraction at the situation of a wide fringe packet induced by the green LED, we proposed a robust surface reconstruction algorithm by combining the simplified moving sine wave fitting (MSWF) based prefiltering and statistic-based phase compensation. The speed of the proposed algorithm can reach to sub-microsecond for one pixel using a laptop. Moreover, the proposed algorithm is suitable for VSI system working at a long coherence length and able to suppress the noise and interference.

2. Background theory

Fig. 1 shows a Mirau-type VSI system, where the light emitted from the incoherent light source is modulated by the Köhler illuminator and then reflected by the beam splitter into the Mirau interferometric objective. In the objective, the light is divided into reference and object beams through the internal splitter. The reflected object and reference beams are recombined followed by passing through the beam splitter and tube lens to produce an interference fringe pattern in a charge coupled device (CCD) camera. Subsequently, the PZT is driven to move the objective vertically for generating a series of interferograms at different optical path differences. The interference signal at each point is demodulated by an VSI algorithm to obtain the vertical positions on the sample surface.

In VSI, the resulting intensity response of a point on the sample along the vertical scanning direction is given by

$$I(z) = I_B + \gamma I_B g(z) \cos\left[\frac{4\pi}{\lambda_0}(z - z_0) + \varphi_0\right], \tag{1}$$

where I_B is the background intensity, γ is the fringe contrast, $g(z)$ is the envelope function of the interference signal, λ_0 is the center wavelength of a light source, z is the vertical scanning position, z_0 is the position where the envelope is maximum and φ_0 is a phase offset introduced by the optical system and surface materials. When a light source with a Gaussian spectrum is used, $g(z)$ is given by

$$g(z) = \exp\left[-4\pi^2\left(\frac{z - z_0}{l_c}\right)^2\right], \tag{2}$$

where $l_c = \lambda_0^2/\Delta\lambda$ is the coherence length of the light source with a spectral bandwidth $\Delta\lambda$. The coherence length l_c is associated with the FWHM of the envelope curve. The modulation amplitude difference between the zero-order fringe and its neighboring order fringes is small under a long l_c, which will reduce the visibility of zero-order fringe and the peakedness of the envelope curve. Therefore, the positioning accuracy of the envelope peak is more susceptible to the scanning step error, low-frequency vibration and other disturbance sources. As a result, the position of envelope peak may bias from the position of the ZOPD (also known as local zero-order fringe peak position) because of the positioning error of envelope peak and systematic phase offset φ_0, see the schematic in Fig. 2. Hence, the positioning accuracy of envelope peak must be improved at first, after which phase compensation should be introduced to accurately determine the position of ZOPD nearest to the envelope peak.

3. Method descriptions

We proposed an algorithm to extract the surface height from the VSI signals with wide fringe packet by accurately locating ZOPD position, and the flowchart of the proposed algorithm is shown in Fig. 3. The algorithm consists of three steps: **Step 1**, filter the original VSI signals of all pixels using simplified MSWF; **Step 2**, extract the envelope curve of filtered signals, and position the envelope peak by parabola fitting and calculate the phase of envelope peak by phase shifting; **Step 3**, Count and correct the phase distribution of envelope peak, then compensate the distribution of peak position by corrected phase distribution and obtain the accurate surface topography. The details of the proposed algorithm are presented in the following sections.

3.1. Signal filtering using simplified moving sine wave fitting

The interference signal at a point along the vertical scanning direction is an amplitude-modulated sine wave. In a full-length interference signal $\{I_0, I_1, I_2, ..., I_{m-1}\}$ with sequence length of m, the amplitude and baseline shift of a section $\mathrm{I}_k = \{I_k, I_{k+1}, I_{k+2}, ..., I_{k+n-1}\}$ are approximately constant especially under a long coherence length. Hence, each value in I_k can be expressed as

$$\begin{aligned} &I_{k+i} = A_k\cos(i\Delta\theta + \varphi_k) + c_k + \varepsilon_{k+i}, \\ &i = 0, 1, ..., n-1; k = 0, 1, ..., m-n, \end{aligned} \tag{3}$$

where A_k, $\Delta\theta$, φ_k, c_k and ε_{k+i} represent the amplitude, the phase step, the initial phase, the baseline shift and the intensity error, respectively. Eq. (3) can also be rewritten as

$$I_{k+i} = a_k\cos(i\Delta\theta) - b_k\sin(i\Delta\theta) + c_k + \varepsilon_{k+i}, \tag{4}$$

in which $a_k = A_k\cos\varphi_k$ and $b_k = A_k\sin\varphi_k$. Thus, the amplitude A_k and initial phase φ_k can be expressed as

$$\begin{cases} A_k = \sqrt{{a_k}^2 + {b_k}^2} \\ \varphi_k = \mathrm{atan2}(b_k, a_k) \end{cases}. \tag{5}$$

The parameters a_k, b_k and c_k can be estimated directly from noisy data by least-square based sine wave fitting [27,28]

$$\begin{bmatrix} a_k \\ b_k \\ c_k \end{bmatrix} = \begin{bmatrix} \sum_{i=0}^{n-1}\cos^2(i\Delta\theta) & -\sum_{i=0}^{n-1}\sin(i\Delta\theta)\cos(i\Delta\theta) & \sum_{i=0}^{n-1}\cos(i\Delta\theta) \\ \sum_{i=0}^{n-1}\sin(i\Delta\theta)\cos(i\Delta\theta) & -\sum_{i=0}^{n-1}\sin^2(i\Delta\theta) & \sum_{i=0}^{n-1}\sin(i\Delta\theta) \\ \sum_{i=0}^{n-1}\cos(i\Delta\theta) & -\sum_{i=0}^{n-1}\sin(i\Delta\theta) & \sum_{i=0}^{n-1}1 \end{bmatrix}^{-1} \begin{bmatrix} \sum_{i=0}^{n-1}I_{k+i}\cos(i\Delta\theta) \\ \sum_{i=0}^{n-1}I_{k+i}\sin(i\Delta\theta) \\ \sum_{i=0}^{n-1}I_{k+i} \end{bmatrix}. \tag{6}$$

When I_k contains several sinusoidal periods integrally, Eq. (6) can be simplified as

$$\begin{aligned} \begin{bmatrix} a_k \\ b_k \\ c_k \end{bmatrix} &= \begin{bmatrix} n/2 & 0 & 0 \\ 0 & -n/2 & 0 \\ 0 & 0 & n \end{bmatrix}^{-1} \begin{bmatrix} \sum_{i=0}^{n-1}I_{k+i}\cos(i\Delta\theta) \\ \sum_{i=0}^{n-1}I_{k+i}\sin(i\Delta\theta) \\ \sum_{i=0}^{n-1}I_{k+i} \end{bmatrix} \\ &= \begin{bmatrix} 2\sum_{i=0}^{n-1}I_{k+i}\cos(i\Delta\theta)\Big/n \\ -2\sum_{i=0}^{n-1}I_{k+i}\sin(i\Delta\theta)\Big/n \\ \sum_{i=0}^{n-1}I_{k+i}\Big/n \end{bmatrix}. \end{aligned} \tag{7}$$

In VSI, the phase step $\Delta\theta$ of interference signal is $\pi/2$, and n will be the multiple of 4. The parameters a_k and b_k can be calculated by

$$\begin{cases} a_k = \dfrac{2}{n}(I_k - I_{k+2} + I_{k+4} - I_{k+6} + \ldots\ldots + I_{k+n-4} - I_{k+n-2}) \\ b_k = -\dfrac{2}{n}(I_{k+1} - I_{k+3} + I_{k+5} - I_{k+7} + \ldots\ldots + I_{k+n-3} - I_{k+n-1}) \end{cases}. \tag{8}$$

We extract one intensity value from every section of interference signal, and the extracted intensity from section I_k can be expressed as

$$I_k{}' = a_k\cos\left(\left(\frac{n}{2}\right)\frac{\pi}{2}\right) - b_k\sin\left(\left(\frac{n}{2}\right)\frac{\pi}{2}\right), k = 0, 1, ..., m-n. \tag{9}$$

According to Eq. (8), Eq. (9) can be rewritten as

$$I_k{}' = \frac{2}{n}\cos(p\pi)\cdot\left(\sum_{j=0}^{p-1}I_{k+4j} - \sum_{j=0}^{p-1}I_{k+4j+2}\right), k = 0, 1, ..., m-n+1, \tag{10}$$

where $p = n/4$ is the number of contained periods in section I_k. The recurrence formula for accelerating calculation is expressed as [29]

$$\begin{aligned} I_{k+4}{}' &= I_k{}' + \frac{2}{n}\cos(p\pi)\left[(I_{k+4p} - I_{k+4p+2}) - (I_k - I_{k+2})\right], k \\ &= 0, 1, ..., m-n-3. \end{aligned} \tag{11}$$

The principle of the interference signal filtering based on the simplified MSWF is shown in Fig. 4, in which the length n of each section is the size of moving window. Eqs. (10) and (11) are used to process each successive section and to acquire the filtered interference signal. Using this method, not only the intensity noise ε_{k+i} can be filtered efficiently, but also the low-frequency drift can be removed since the local baseline shift c_k of section I_k is ditched in Eq. (10).

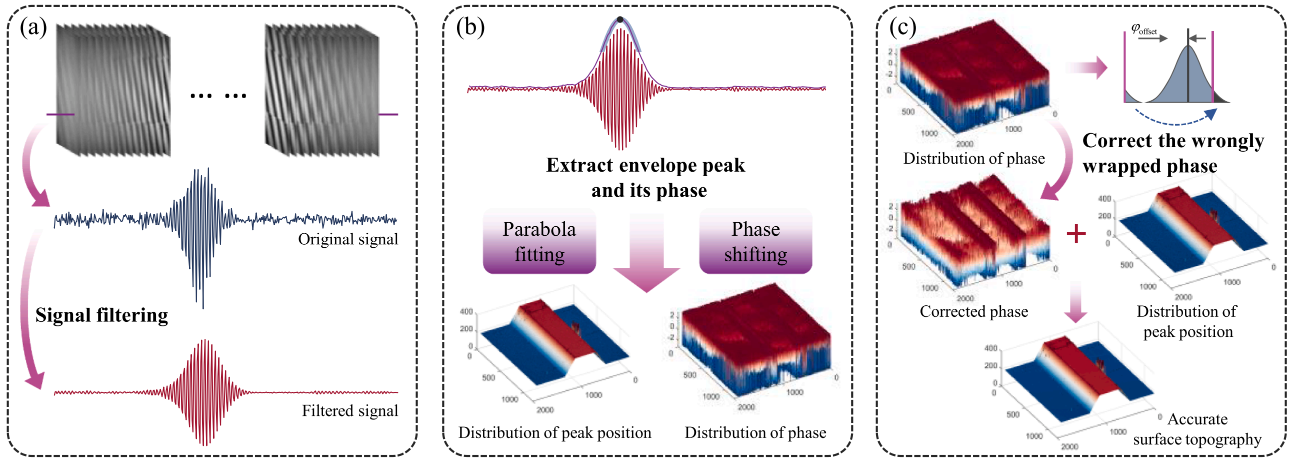

Fig. 3. Flowchart of the proposed algorithm.

3.2. Envelope peak extraction based on parabola fitting

The three consecutive points in a filtered interference signal can be expressed as

$$\begin{cases} I'_{k-1} = A_{k-1}\cos\left(\varphi_k - \dfrac{\pi}{2}\right) = A_{k-1}\sin\varphi_k \\ I'_k = A_k\cos\varphi_k \\ I'_{k+1} = A_{k+1}\cos\left(\varphi_k + \dfrac{\pi}{2}\right) = -A_{k+1}\sin\varphi_k \end{cases}, \tag{12}$$

where we have

$$A_{k-1} \approx A_k \approx A_{k+1}. \tag{13}$$

Hence, the amplitude A_k and initial phase φ_k of I'_k can be expressed as

$$A_k = \sqrt{\left({I'_{k-1}}^2 + 2{I'_k}^2 + {I'_{k+1}}^2\right)/2}, \tag{14}$$

$$\varphi_k = \operatorname{atan2}(I'_{k-1} - I'_{k+1}, 2I'_k). \tag{15}$$

According to Eq. (14), the amplitude envelope curve can be calculated. In order to reduce computation time, we do not take logarithm for the amplitude envelope. The shape of the envelope $\mathbf{A}_{k_{\max}} = \{A_{k_{\max}-f_w}, \ldots, A_{k_{\max}}, \ldots, A_{k_{\max}+f_w}\}$ around the peak value $A_{k_{\max}}$ of the amplitude envelope is close to a parabola, thus parabola fitting was utilized in this paper. f_w is the half-width of fitting range, which should be properly chosen for balancing computation time and calculation precision. The parabolic equation is given by

$$f(k) = \alpha_1 k^2 + \alpha_2 k + \alpha_3, \tag{16}$$

the fitted coefficients of envelope section $\mathbf{A}_{k_{\max}}$ obtained by least squares approach can be expressed as

$$\begin{bmatrix} \alpha_1 \\ \alpha_2 \\ \alpha_3 \end{bmatrix} = \begin{bmatrix} \sum_{k=-f_w}^{f_w} k^4 & 0 & \sum_{k=-f_w}^{f_w} k^2 \\ 0 & \sum_{k=-f_w}^{f_w} k^2 & 0 \\ \sum_{k=-f_w}^{f_w} k^2 & 0 & \sum_{k=-f_w}^{f_w} 1 \end{bmatrix}^{-1} \begin{bmatrix} \sum_{k=-f_w}^{f_w} A_k k^2 \\ \sum_{k=-f_w}^{f_w} A_k k \\ \sum_{k=-f_w}^{f_w} A_k \end{bmatrix}. \tag{17}$$

Hence, the parabola peak that represents the envelope peak can be positioned at

$$k_{\text{peak}} = k_{\max} - \frac{\alpha_2}{2\alpha_1}. \tag{18}$$

In general, k_{peak} is calculated as decimal. k_{peak} can be rewritten as

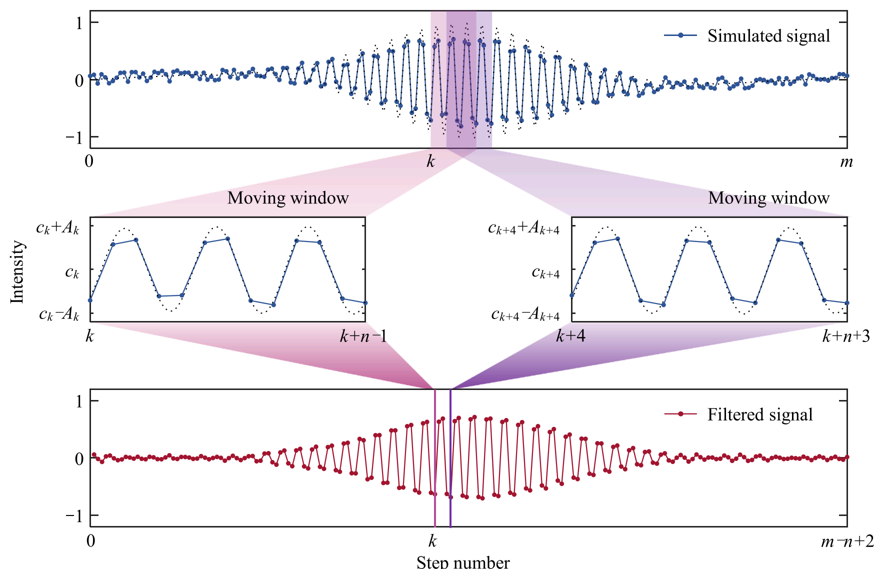

Fig. 4. Schematic diagram of the MSWF process.

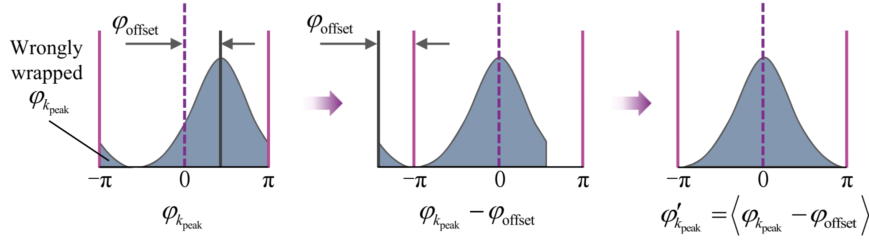

Fig. 5. Illustration of the phase correction for wrongly wrapped $\varphi_{k_{peak}}$.

$$k_{peak} = k_{int} + k_{dec}, \tag{19}$$

where, k_{int} and k_{dec} represent the integer part and the decimal part of the envelope peak position k_{peak}, respectively. $k_{int} = \lfloor k_{peak} + 0.5 \rfloor$, where $\lfloor \cdot \rfloor$ denotes round down.

3.3. ZOPD locating by phase compensation of envelope peak position

The wrapped phase at envelope peak position k_{peak} can be obtained by combining Eq. (15) and Eq. (19), i.e.

$$\varphi_{k_{peak}} = \left\langle \mathrm{atan2}\left(I'_{k_{int}-1} - I'_{k_{int}+1}, 2I'_{k_{int}}\right) + \frac{\pi}{2} k_{dec} \right\rangle, \tag{20}$$

where, $\langle \cdot \rangle$ denotes wrapping the angles to the interval $[-\pi, \pi]$, which is necessary after compensating the phase of k_{int} using k_{dec} due to the range of atan2 is $[-\pi, \pi]$.

Theoretically, the position of envelope peak k_{peak} relative to ZOPD obey normal distribution due to random error of peak positioning, especially for sample with smooth and flat surface. If the positioning of envelope peak is accurate enough to ensure that the distribution width of the position of envelope peak k_{peak} relative to ZOPD is smaller than 4, namely one period of 2π in phase, the wrapped phase $\varphi_{k_{peak}}$ at the envelope peak will also be normally distributed, but $\varphi_{k_{peak}}$ may be wrongly wrapped in $[-\pi, \pi]$ because of phase offset φ_0. In the imaging area of camera, the wrapped phase $\varphi_{k_{peak}}$ of envelope peak position in all pixel coordinates can be used for generating a histogram, as shown in Fig. 5. The top position φ_{offset} of the histogram is approximately the phase offset φ_0 in Eq. (1). In order to minimize the number of wrongly wrapped $\varphi_{k_{peak}}$ at each pixel, φ_{offset} must be subtracted from $\varphi_{k_{peak}}$, and then rewrapping $\varphi_{k_{peak}} - \varphi_{offset}$. Thus, the symmetric distributed $\varphi'_{k_{peak}}$ can be obtained by

$$\varphi'_{k_{peak}} = \left\langle \varphi_{k_{peak}} - \varphi_{offset} \right\rangle. \tag{21}$$

Obviously, if the original distribution width of $\varphi_{k_{peak}}$ is less than 2π, all the wrapped $\varphi_{k_{peak}}$ caused by φ_{offset} eccentricity can be corrected. Otherwise, the 2π phase jump will appear in a few pixels.

Therefore, the ZOPD position of a point on (x, y) can be calculated by

$$k_{ZOPD}(x, y) = k_{peak}(x, y) - \left(\varphi_{offset} + \varphi'_{peak}(x, y)\right) \frac{2}{\pi}, \tag{22}$$

where φ_{offset} is not necessary for the recovery of relative height but it is meaningful for determining exact ZOPD position without systematic deviation. Finally, the surface height can be expressed as

$$h(x, y) = k_{ZOPD}(x, y) \times \frac{\lambda_0}{8}. \tag{23}$$

4. Simulation

In order to compare the performance of the proposed algorithm with conventional five-bucket WLPSI and Hilbert transform algorithms, numerical simulation was carried out. The discrete intensity signal of a point in a white light interferogram can be expressed as [1]

$$I_k = 100 + 100\exp\left[-\frac{(k-200)^2 \Delta z^2}{\sigma^2}\right] \cos\left[\frac{4\pi}{\lambda_0}(k-200)\Delta z + \varphi_0\right], \tag{24}$$

where $\sigma = l_c/2\pi$, k is the step number, Δz is the scanning interval 65 nm, λ_0 is the center wavelength 520 nm, φ_0 is an additional phase term, which is set to $\pi/2$. The envelope peak of the simulated signal locates at $k = 200$, and the corresponding surface height is 13 μm. Algorithms were implemented using MATLAB installed on a laptop (i5–10210 U CPU, 16 GB RAM). For an intensity signal with whose length of 400, the computation time of the proposed algorithm, conventional WLPSI and Hilbert transform algorithm is 0.657 μs, 0.269 μs and 34.618 μs, respectively. The Hilbert transform is very time consuming due to the convolution operation [30], while the two others are much faster.

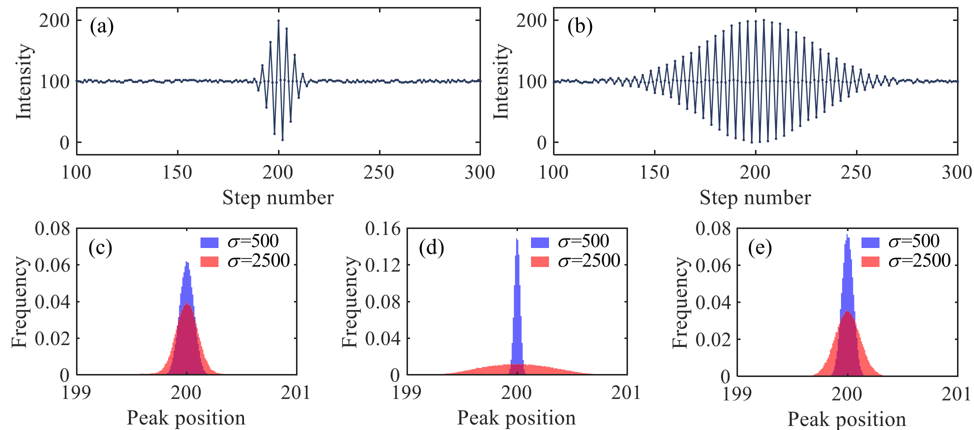

Fig. 6. Statistical distribution of the envelope peak under different σ. (a) and (b) are the simulated VSI signals at $\sigma = 500$ nm and $\sigma = 2500$ nm, respectively. (c), (d) and (e) are the histograms of envelope peak positions extracted by the proposed algorithm, the conventional WLPSI and the Hilbert transform.

Table 1
SDs of the calculated heights by using the three algorithms at different σ.

σ (nm)	SDs (nm)		
	Proposed method	Conventional WLPSI	Hilbert transform
500	0.2905	2.6161	3.2757
1000	0.2070	11.7075	4.3481
1500	0.1664	20.7408	5.7124
2000	0.1442	23.4080	6.6011
2500	0.1295	27.3189	7.5081

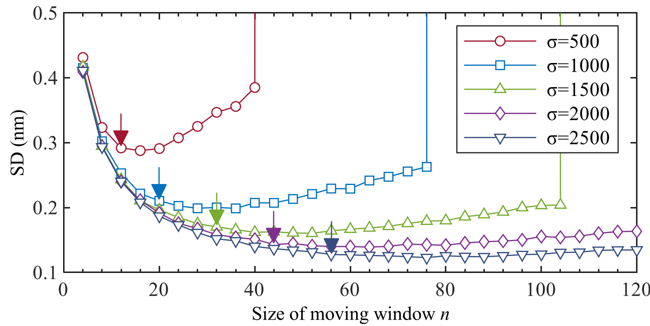

Fig. 7. SDs of the calculated heights by using the proposed algorithm with different moving windows.

4.1. Effect of coherence length on measurement accuracy

The FWHM of envelope curve is determined by the coherence length, which affects the positioning accuracy of envelope peak. To validate this, random noise at the level of 5 % generated within the range [−2.5, 2.5] is added to the modelled discrete VSI signal. As can be seen in Fig. 6 (a) and 6(b), the FWHW of the envelope curve is wider under a higher σ, and the FWHW is directly proportional to σ. One hundred thousand sets of VSI signals are generated for repetitive calculation. Figs. 6(c-e) show the normalized histogram of envelope peak positions calculated by the proposed method, WLPSI and Hilbert transform, respectively. It can be observed that the peak positioning accuracy of three methods decreases when σ increases, particularly the conventional WLPSI. The conventional WLPSI presents the best accuracy of peak positioning only in the shortest coherence length. For Hilbert transform, the extracted position of envelope peak is regarded as the ZOPD position, which is then used for surface height recovery directly, while the envelope peak positions need to be corrected further to determine the ZOPD position in the two other algorithms, i.e., our proposed algorithm and the conventional WLPSI.

Table 1 shows the SDs of the calculated heights by the three aforementioned algorithms at different σ. As has been estimated, SD increases with σ for conventional WLPSI and Hilbert transform. Because the positioning accuracy of envelope peak using conventional WLPSI decreases dramatically under higher σ, the extracted envelope peak may deviate from ZOPD position heavily, which may reduce the calculation accuracy of five-bucket phase shifting for extracting wrapped phase of envelope peak. As a result, the positioning accuracy of ZOPD is very low even the phase compensation is applied. However, the SD decreases when σ increases for the proposed method. This can be explained as follows: The moving window size n of the simplified MSWF and the fitting range of the parabola fitting can be selected appropriately under different σ, in order to maintain the positioning accuracy of envelope peak as much as possible. Besides, the phase of envelope peak $\varphi_{k_{\mathrm{peak}}}$ can be calculated more precisely because of the higher degree of approximation in Eq. (13). After trying different window sizes for the interference signals generated under different σ, we empirically found that the distance between two inflection point in the Gaussian envelope curve can be regarded as an appropriate size for the moving window, which can be calculated by

$$n = 4\cdot\left\lfloor \frac{\sqrt{2}\sigma}{4\Delta z} + 0.5 \right\rfloor. \tag{25}$$

Fig. 7 shows the SDs of the reconstructed heights at different σ when using the simplified MSWF with different window size n. The arrow "↓" indicates the optimum window size n calculated by empirical Eq. (25),

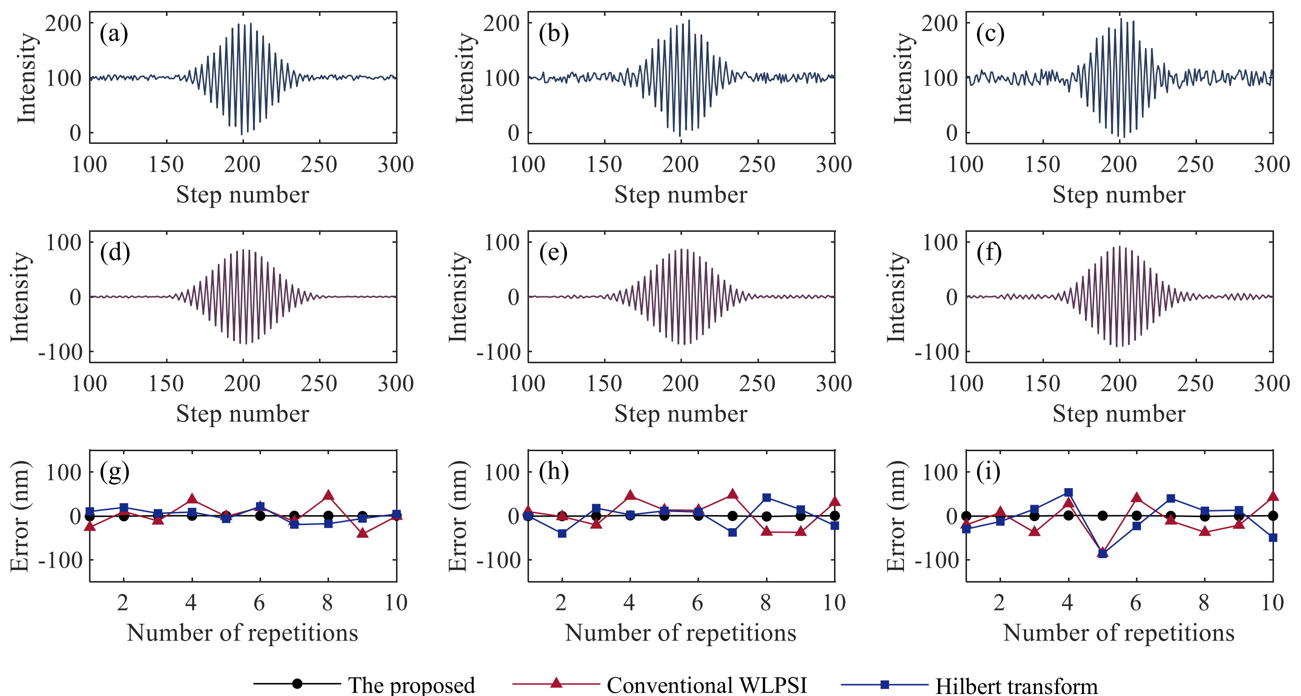

Fig. 8. Simulated results under different noise levels. The simulated VSI signals under (a) 10 %, (b) 20 % and (c) 30 % random noises, respectively. (d), (e) and (f) are the corresponding filtered signals using simplified MSWF with window size $n = 8$. (g), (h) and (i) are the corresponding errors using three different algorithms.

Table 2
SDs of the calculated heights by using the three algorithms under different levels of random intensity noise.

Noise level	SDs (nm)		
	Proposed method	Conventional WLPSI	Hilbert transform
0 %	0	0	0
5 %	0.1672	20.8774	5.8107
10 %	0.3394	26.9825	11.2260
15 %	0.5056	28.5006	16.7590
20 %	0.6907	30.8412	23.2956
25 %	0.8445	36.5085	29.5882
30 %	1.0226	43.3844	37.6374

where the window size n is as small as possible and SD is also small.

4.2. Effect of intensity noise and baseline drift on the measurement accuracy

To investigate the anti-noise capability of the three aforementioned algorithms, the discrete VSI signals superimposed with random intensity noise at different levels are generated under σ of 1500 nm, as shown in Figs. 8(a-c). The corresponding filtered signals are shown in Figs. 8(d-f), it can be seen that the simplified MSWF with window size $n = 8$ is still effective for fitting the signals at $\sigma = 1500$ nm with 30 % random noise. The VSI signal is rough and the zero-order fringe peak cannot be recognized directly at higher noise levels, in which case the positioning accuracy of envelope peak will be affected, and ultimately influence the accuracy of surface height reconstruction. After calculating 10 times of surface height by using different algorithms, the corresponding results of absolute height errors in simulations are shown in Figs. 8(g-i). There is a slight change in the absolute height errors introduced by the conventional WLPSI and Hilbert transform methods once 10 % noise was added, while the measurement results achieved by the proposed method remain almost constant. When the noise level increases to 30 %, the absolute height errors introduced by the conventional WLPSI and Hilbert transform methods increase significantly. In contrast, the proposed algorithm remains at a high accuracy even the noise level is increased up to 30 %. Table 2 shows the SDs of obtained height by different algorithms under different noise levels. The proposed algorithm shows strong noise immunity compared with the other two algorithms. It should be emphasized that although a wider moving window of simplified MSWF can be applied to filter the noise with much higher levels, the moving window should not be too wide otherwise the flat top will appear in the envelope curve.

Under 5 % random noise and $\sigma = 1500$ nm, a series of VSI signals is generated with linear, sinusoidal and mixed drift, as shown in Figs. 9(a-c). Fig. 9(d) represents the VSI signal after filtering the signal in Fig. 9(c) using the simplified MSWF. The SDs of heights obtained by the three algorithms are shown in Table 3. It can be observed that the results of proposed algorithm unaffected by the low-frequency baseline drift on the strength of simplified MSWF. However, the conventional WLPSI is distinctly affected by the sinusoidal and mixed drift, while the Hilbert transform is affected by the linear and mixed drift slightly.

4.3. Effect of PZT's positioning noise on the measurement accuracy

In a VSI system, the PZT drives the objective to scan at a certain phase interval. As a result, the positioning error of the PZT scanner affects the calculation of the envelope peak from the interferogram

Table 3
SDs of the calculated heights by using the three algorithms under different types of baseline drift.

Drift type	SDs (nm)		
	Proposed method	Conventional WLPSI	Hilbert transform
/	0.1672	20.8774	5.8107
Linear	0.1669	21.7675	6.2317
Sinusoidal	0.1656	25.1639	5.7850
Mixed	0.1683	26.1236	6.2678

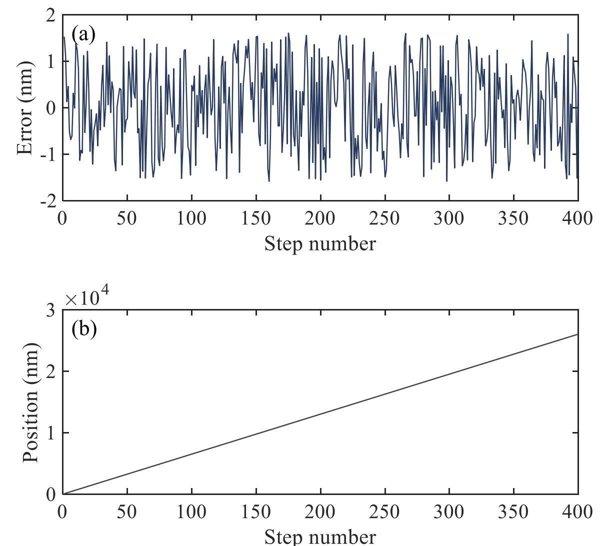

Fig. 10. (a) Random error of scanning interval and (b) the scanning position as a function of the step number.

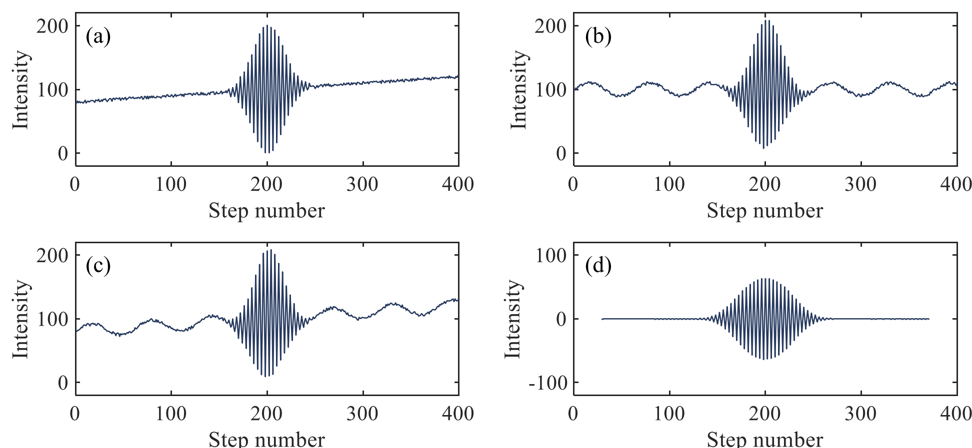

Fig. 9. Simulated VSI signals with different types of baseline drift: (a) linear; (b) sinusoidal; (c) mixed. (d) is the filtered signal of (c).

Table 4
SDs of the calculated heights by using the three algorithms under different levels of random positioning noise.

Noise level	SDs (nm)		
	Proposed method	Conventional WLPSI	Hilbert transform
0 %	0.1789	20.8285	5.8512
1 %	2.5965	21.4979	5.8187
2 %	5.2331	24.0744	7.6799
3 %	7.8454	26.6736	9.9350
4 %	10.2832	29.5434	12.2023
5 %	13.0243	31.0264	13.9755

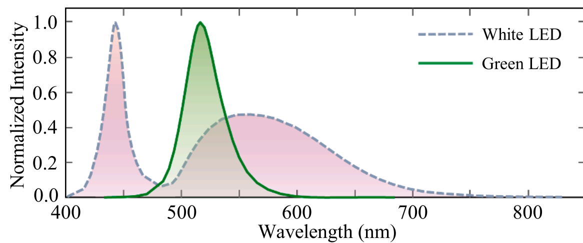

Fig. 11. Normalized spectral power distribution of the White and Green LED.

sequence [8], which will further degenerate the reconstruction accuracy for surface height. The random errors of PZT are shown in Fig. 10(a) under the maximum mechanical position noise at level of 5 % within the range of [−2.5 %Δz, 2.5 %Δz], and the scanning position of PZT is shown in Fig. 10(b). Different levels of positioning noise and a 5 % random intensity noise were added into a series of simulated VSI signals. The SDs of the reconstructed heights by the three aforementioned algorithms are shown in Table 4, in which we can find that the SDs of the three algorithms increase with the noise level of PZT positioning. However, our algorithm still outperforms the other two even if the noise level is as larger as 5 %. As for the higher level of PZT positioning noise, the uncertain scanning step and inaccurate spatial sampling shifts and disrupts the fringe packet in the signal sequence, which is hard to be compensated by most of the algorithms. Here we should emphasize that the positioning noise of some commercial PZT scanner can reach up to 0.1 nm, which is much more accurate that the modelled cases (i.e., 5 % positioning noise level) in Table 4. Therefore, we claim that our algorithm is more robust for PZT positioning error than the other two algorithms.

5. Experiments

An VSI system consisting of a Mirau-type objective (NA 0.4, Magnification 20 ×) and a CMOS camera (IDS, UI-3160 CP-M-GL) is used to capture the interferogram. The objective is mounted on a PZT scanner (PI, P-725.4CDE2) with travel range of 400 μm and position noise of 0 .1nm. The PZT scanner is controlled by a PZT digital controller (PI, E-754K.1CD). A green LED (CCS, HLV3–22GR-4S) with unimodal spectral distribution is applied for illuminating the sample, whose normalized intensity spectrum is shown in Fig. 11. The center wavelength λ_0 was measured to be 546 nm and the coherence length l_c was estimated at 10.5 μm. The scanning interval Δz is set as 68.25 nm, and the size of moving window n as well as the half-width of parabola fitting range f_w are set as 36 and 15, respectively.

In order to show the accuracy of the constructed VSI system with our proposed algorithm, a 12 μm standard step sample (11.97 ± 0.05 μm)

Table 5
Comparison for the reconstructed heights of the standard step sample using the three algorithms.

Results	Proposed method (μm)	Conventional WLPSI (μm)	Hilbert transform (μm)
1	11.9791	11.8821	12.0123
2	11.9778	12.0287	12.0173
3	11.9816	11.9779	11.9854
4	11.9792	11.9861	12.0142
5	11.9790	11.6594	11.9764
6	11.9796	12.0963	12.0406
7	11.9771	12.0498	12.0301
8	11.9824	12.2932	12.0530
9	11.9792	11.7799	11.9488
10	11.9803	11.8133	11.9814
Average height	11.9795	11.9567	12.0059
SD	0.00151	0.17135	0.03065

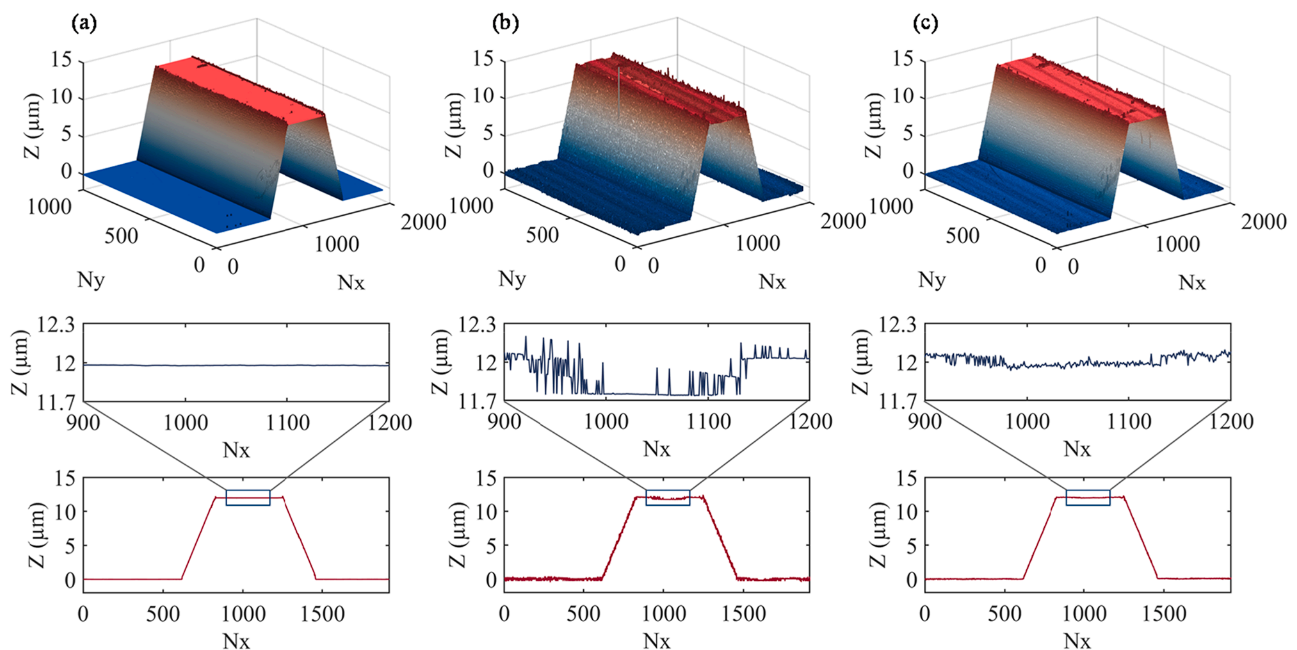

Fig. 12. Reconstruction results for a standard step sample using (a) the proposed method, the (b) conventional WLPSI, and the (c) Hilbert transform.

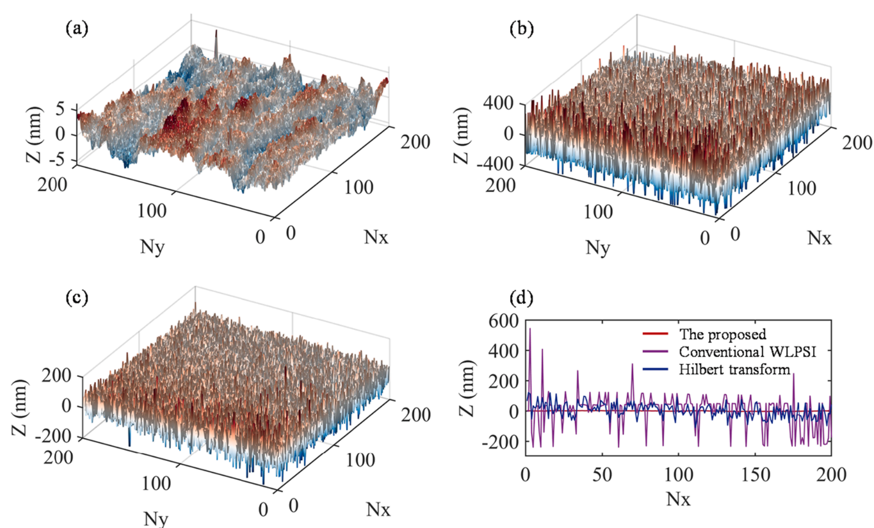

Fig. 13. Reconstruction results of a single crystal silicon wafer using the (a) proposed method, the (b) conventional WLPSI, and the (c) Hilbert transform. (d) is the 2D cross-section profile.

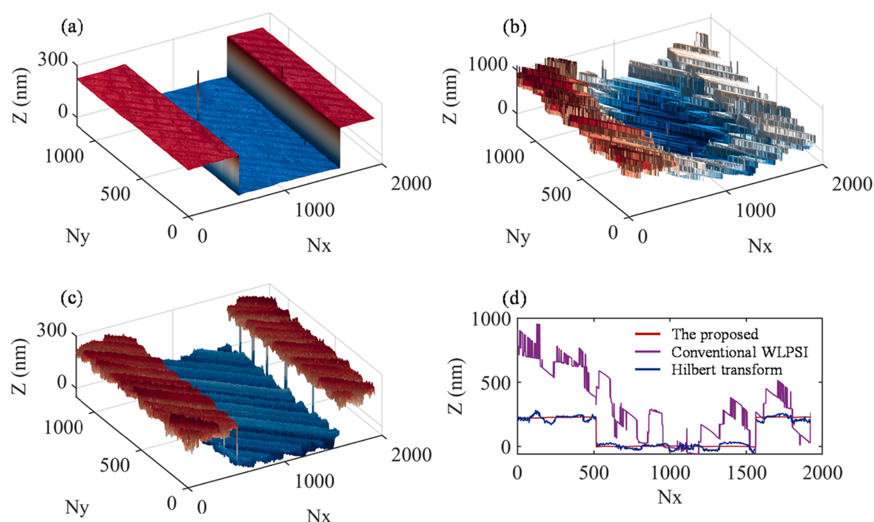

Fig. 14. Reconstruction results of an in-house etched groove using the (a) proposed method, the (b) conventional WLPSI, and the (c) Hilbert transform. (d) is the 2D cross-section profile.

calibrated by the Mahr company was measured by 10 times in a static environment. The 3D profile as well as a cross-section of the profile by the aforementioned three algorithms are shown in Fig. 12. It can be seen that the proposed algorithm demonstrates the most accurate results. As a comparison, the profiles reconstructed by the other two algorithms show many discontinuities and burrs, which is especially the case for conventional WLPSI. Table 5 presents the evaluated height values according to ISO 5436–1 as well as the average heights and the SDs. Apparently, the proposed algorithm demonstrates the most accurate averaged height (11.9795 μm) as well as the smallest SD (0.00151 μm) when compared to the others, which verifies the accuracy and repeatability of the proposed algorithm in this paper. Here we should emphasize that the reconstructed height by the proposed method may be further improved by calibrating the center wavelength λ_0 of the green LED.

A silicon wafer with a 0.38 nm *Sa* and a 1.07 nm *Sq*, determined by a commercial VSI (ATOMETRICS, EX230) according to ISO 25,178, was measured to evaluate the three algorithms. The reconstruction results after leveling are shown in Fig. 13. Obviously, there are dense burrs with whose height are tens or hundreds of nanometers in the 3D profile using WLPSI and Hilbert transform, which is caused by the inaccurate detection of envelope peak under a wider envelope curve. Hence, the two algorithms can hardly measure a structure with nanoscale height distribution. In contrast, the 3D profile fluctuates within ±5 nm using the proposed algorithm, and the *Sa* as well as the *Sq* of reconstructed surface are 0.35 nm and 0.79 nm, respectively. In addition, an in-house etched rectangular groove with a 229.9 nm depth (according to ISO 5436–1) measured by the commercial VSI was remeasured using the VSI system. The reconstruction results after leveling are shown in Fig. 14. It can be seen that the conventional WLPSI and the Hilbert transform cannot accurately reconstruct the profile of the rectangular groove. This indicates the envelope peak detection method in the conventional WLPSI and the phase compensation in the determination of ZOPD fail at the condition of a light source with a long coherence length. While for the Hilbert transform without phase compensation, the detection of the envelope peak is inaccurate to reconstruct the profile of the groove. As a comparison, the proposed algorithm accurately reconstructed the profile of the groove, whose measured depth is 227.8 nm. The aforementioned results demonstrate that the proposed method outperforms the conventional algorithms in terms of robustness and accuracy at the condition of a light source with a long coherence length.

6. Conclusion

In this paper, a robust surface recovery algorithm is proposed for a green LED-based VSI. The simulated results demonstrate that the proposed algorithm is much more accurate in ZOPD positioning and much more robust against noises over the conventional WLPSI and Hilbert transform at a long coherence length. A VSI system is constructed to verify the performance of the proposed algorithm by measuring three samples, i.e., a 12 μm standard step sample, a silicon wafer, and an in-house etched groove. Our measured results show that the height of the standard step sample is 11.9795 μm, the roughness *Sa* of the silicon wafer is 0.35 nm, and the groove depth of the in-house etched groove is 227.8 nm, which are comparable to the measured values by a commercial VSI system. Furthermore, the measured SDs for the standard step sample using the proposed algorithm, conventional WLPSI and Hilbert transform are 1.5 nm, 171.4 nm and 30.7 nm respectively. This demonstrates the high robustness of our algorithm against random and system noises when using a light source with a long coherence length.

CRediT authorship contribution statement

Hang Zhao: Writing – original draft, Software, Methodology, Formal analysis. **Yijun Xie:** Resources, Investigation. **Renlong Zhu:** Validation, Resources. **Zhengqiong Dong:** Supervision, Resources. **Xuanze Wang:** Methodology, Conceptualization. **Shiyuan Liu:** Methodology, Conceptualization. **Jinlong Zhu:** Writing – review & editing, Project administration.

Declaration of competing interest

The authors declare that they have no known competing financial interests or personal relationships that could have appeared to influence the work reported in this paper.

Funding

This work was funded by the National Nature Science Foundation of China (Grant No. 52175509), the National Key Research and Development Program of China (2023YFF1500900), the Shenzhen Fundamental Research Program (JCYJ20220818100412027), the Guangdong-Hong Kong Technology Cooperation Funding Scheme Category C Platform (SGDX20230116093543005), and the Innovation Project of Optics Valley Laboratory (Grant No. OVL2023PY003).

Data availability

Data will be made available on request.

References

[1] Vo Q, Fang F, Zhang X, Gao H. Surface recovery algorithm in white light interferometry based on combined white light phase shifting and fast Fourier transform algorithms. Appl Opt 2017;56:8174. https://doi.org/10.1364/AO.56.008174.
[2] Zhu J, Liu J, Xu T, Yuan S, Zhang Z, Jiang H, et al. Optical wafer defect inspection at the 10 nm technology node and beyond. Int J Extreme Manuf 2022;4:032001. https://doi.org/10.1088/2631-7990/ac64d7.
[3] Chen W, Liu S, Zhu J. Pixelated non-volatile programmable photonic integrated circuits with 20-level intermediate states. Int J Extreme Manuf 2024;6:035501. https://doi.org/10.1088/2631-7990/ad2c60.
[4] Zhang J, Tan KL, Hong GD, Yang LJ, Gong HQ. Polymerization optimization of SU-8 photoresist and its applications in microfluidic systems and MEMS. J Micromechanics Microengineering 2001;11:20–6. https://doi.org/10.1088/0960-1317/11/1/304.
[5] Hansen HN, Carneiro K, Haitjema H, De Chiffre L. Dimensional micro and nano metrology. CIRP Ann 2006;55:721–43. https://doi.org/10.1016/j.cirp.2006.10.005.
[6] Su R, Wang Y, Coupland J, Leach R. On tilt and curvature dependent errors and the calibration of coherence scanning interferometry. Opt Express 2017;25:3297. https://doi.org/10.1364/OE.25.003297.
[7] Yang S, Zhang G. A review of interferometry for geometric measurement. Meas Sci Technol 2018;29:102001. https://doi.org/10.1088/1361-6501/aad732.
[8] Chen W, Xiong Y, Chen J, Chen S. Accurate white light phase-shifting interferometry under PZT scanning error. Opt Lasers Eng 2023;169:107728. https://doi.org/10.1016/j.optlaseng.2023.107728.
[9] Harasaki A, Schmit J, Wyant JC. Improved vertical-scanning interferometry. Appl Opt 2000;39:2107. https://doi.org/10.1364/AO.39.002107.
[10] Guo T, Li F, Chen J, Fu X, Hu X. Multi-wavelength phase-shifting interferometry for micro-structures measurement based on color image processing in white light interference. Opt Lasers Eng 2016;82:41–7. https://doi.org/10.1016/j.optlaseng.2016.02.003.
[11] Zhai Z, Zhang Y, Wang X, Dong Z, Cheng Z, Lv Q, et al. Alignment of the initial phase during multiple-wavelength switching in microscopic interferometry. Opt Laser Technol 2019;115:493–9. https://doi.org/10.1016/j.optlastec.2019.02.059.
[12] Li M, Quan C, Tay CJ. Continuous wavelet transform for micro-component profile measurement using vertical scanning interferometry. Opt Laser Technol 2008;40:920–9. https://doi.org/10.1016/j.optlastec.2008.01.013.
[13] Shen MH, Hwang CH, Wang WC. Using higher steps phase-shifting algorithms and linear least-squares fitting in white-light scanning interferometry. Opt Lasers Eng 2015;66:165–73. https://doi.org/10.1016/j.optlaseng.2014.09.004.
[14] Cui K, Liu Q, Huang X, Zhang H, Li L. Scanning error detection and compensation algorithm for white-light interferometry. Opt Lasers Eng 2022;148:106768. https://doi.org/10.1016/j.optlaseng.2021.106768.
[15] Sinclair MB, De Boer MP, Corwin AD. Long-working-distance incoherent-light interference microscope. Appl Opt 2005;44:7714. https://doi.org/10.1364/AO.44.007714.
[16] Xin L, Dou J, Yang Z, Liu Z. Composite wavelet decomposition algorithm combined with correlation analysis in white-light scanning interferometry. Results Phys 2022;40:105870. https://doi.org/10.1016/j.rinp.2022.105870.
[17] Lehmann P, Kühnhold P, Xie W. Reduction of chromatic aberration influences in vertical scanning white-light interferometry. Meas Sci Technol 2014;25:065203. https://doi.org/10.1088/0957-0233/25/6/065203.
[18] Lehmann P. Vertical scanning white-light interference microscopy on curved microstructures. Opt Lett 2010;35:1768. https://doi.org/10.1364/OL.35.001768.
[19] Lehmann P, Tereschenko S, Xie W. Fundamental aspects of resolution and precision in vertical scanning white-light interferometry. Surf Topogr Metrol Prop 2016;4:024004. https://doi.org/10.1088/2051-672X/4/2/024004.
[20] Zhu L, Dong Y, Li Z, Zhang X. A novel surface recovery algorithm for dual wavelength white LED in vertical scanning interferometry (VSI). Sensors 2020;20:5225. https://doi.org/10.3390/s20185225.
[21] Chong WK, Li X, Soh YC. Spectral effects of dual wavelength low coherence light source in white light interferometry. Opt Lasers Eng 2013;51:651–5. https://doi.org/10.1016/j.optlaseng.2012.12.014.
[22] Chen S, Palmer AW, Grattan KTV, Meggitt BT. Fringe order identification in optical fibre white-light interferometry using centroid algorithm method. Electron Lett 1992;28:553. https://doi.org/10.1049/el:19920349.
[23] De Groot P, Colonna De Lega X. Signal modeling for low-coherence height-scanning interference microscopy. Appl Opt 2004;43:4821. https://doi.org/10.1364/AO.43.004821.
[24] Park MC. Direct quadratic polynomial fitting for fringe peak detection of white light scanning interferograms. Opt Eng 2000;39:952. https://doi.org/10.1117/1.602445.
[25] Chim SSC, Kino GS. Phase measurements using the Mirau correlation microscope. Appl Opt 1991;30:2197. https://doi.org/10.1364/AO.30.002197.
[26] Pavliček P, Michálek V. White-light interferometry—Envelope detection by Hilbert transform and influence of noise. Opt Lasers Eng 2012;50:1063–8. https://doi.org/10.1016/j.optlaseng.2012.02.008.
[27] Wang X., Luo Y., Zhai Z., Yang L., He T. Algorithm for sine wave cure fit based on frequency precise estimation, 2017, p. 357–61. https://doi.org/10.1109/ICMSC.2017.7959501.
[28] Liu X, Ren Y, Chu C, Fang W. Accurate frequency estimation based on three-parameter sine-fitting with three FFT samples. Metrol Meas Syst 2015;22:403–16. https://doi.org/10.1515/mms-2015-0032.
[29] Wang X, Wang A, Yin J, Zhao H, Dong Z, Fan Y, et al. Improved measurement accuracy based on moving sine-wave fitting for ultrasonic ranging. Shock Vib 2022;2022:1–7. https://doi.org/10.1155/2022/9570857.
[30] Wu D, Liang F, Kang C, Fang F. Performance analysis of surface reconstruction algorithms in vertical scanning interferometry based on coherence envelope detection. Micromachines 2021;12:164. https://doi.org/10.3390/mi12020164.